

Momentum-space imaging spectroscopy for the study of nanophotonic materials

Yiwen Zhang^{a,c}, Maoxiong Zhao^{a,d}, Jiajun Wang^{a,d}, Wenzhe Liu^{a,d}, Bo Wang^{a,d}, Songting Hu^b, Guopeng Lu^b, Ang Chen^b, Jing Cui^b, Weiyi Zhang^b, Chia Wei Hsu^c, Xiaohan Liu^{a,d}, Lei Shi^{a,b,d,*}, Haiwei Yin^{b,*}, Jian Zi^{a,d,*}

^aDepartment of Physics, Key Laboratory of Micro- and Nano-Photonic Structures (Ministry of Education), and State Key Laboratory of Surface Physics, Fudan University, Shanghai 200433, China

^bShanghai Engineering Research Center of Optical Metrology for Nano-fabrication (SERCOM), Shanghai 200433, China

^cMing Hsieh Department of Electrical Engineering, University of Southern California, Los Angeles, CA 90089, USA

^dCollaborative Innovation Center of Advanced Microstructures, Fudan University, Shanghai 200433, China

Abstract

The novel phenomena in nanophotonic materials, such as the angle-dependent reflection and negative refraction effect, are closely related to the photonic dispersions $E(\mathbf{p})$. $E(\mathbf{p})$ describes the relation between energy E and momentum \mathbf{p} of photonic eigenmodes, and essentially determines the optical properties of materials. As $E(\mathbf{p})$ is defined in momentum space (k -space), the experimental method to detect the energy distribution, that is the spectrum, in a momentum-resolved manner is highly required. In this review, the momentum-space imaging spectroscopy (MSIS) system is presented, which can directly study the spectral information in momentum space. Using the MSIS system, the photonic dispersion can be captured in one shot with high energy and momentum resolution. From the experimental momentum-resolved spectrum data, other key features of photonic eigenmodes, such as quality factors and polarization states, can also be extracted through the post-processing algorithm based on the coupled mode theory. In addition, the interference configurations of the MSIS system enable the measurement of coherence properties and phase information of nanophotonic materials, which is important for the study of light-matter interaction and beam shaping with nanostructures. The MSIS system can give the comprehensive information of nanophotonic materials, and is greatly useful for the study of novel photonic phenomena and the development of nanophotonic technologies.

Keywords:

Momentum space imaging, nanophotonic material, photonic dispersion, photonic eigenmode, quality factor, polarization state

1. Introduction

The study of nanophotonic materials has become a vibrant multidisciplinary field, providing opportunities and challenges for both fundamental and applied research. Nanophotonic materials, such as photonic crystals (PhCs) [1–4], plasmonic structures [5–9] and metamaterials [10–14], are composed of micro-nano structures, which can mold the motion of photons at a wavelength or even subwavelength scale, giving us the fascinating new ways to control light. In photonic systems, the states of motion of photons, that is photonic eigenmodes, are labelled by photon energy E and momentum \mathbf{p} . The dependence of E on \mathbf{p} , known as photonic dispersion $E(\mathbf{p})$, describes the energy levels of photonic eigenmodes in momentum space. Photonic dispersions determine the material's responses to the external light fields, and result in a variety of novel phenomena in nanophotonic materials. For example, the angle-dependent reflection effect of three-dimensional PhCs [15, 16] is originated from photonic band gaps (PBGs) in their dispersions; and the negative refraction effect in metamaterials [10] is a result of the negative dispersion band curvature. The photonic dispersion

engineering provides an exquisite control over the propagation and localization of photons, driving novel applications in solid-state lighting [17–19], new generation energy technology [20–22], optical sensing [4, 23, 24] and optical computing [25–28]. The comprehensive investigation of photonic dispersion information has played a key role for the fundamental research, such as the study of light-matter interactions [29, 30], topological photonics [31–38] and non-Hermitian photonics [39–41].

Since the photon energy E is directly proportional to its frequency ω , it is essential to detect the frequency distribution, that is spectrum, in a momentum-resolved manner for the investigation of $E(\mathbf{p})$. As yet there are several methods introduced for the momentum-resolved spectrum measurement. One method is using the phase-sensitive heterodyne near-field optical microscope [42, 43], where both intensity and phase of near fields can be detected by a complicated integration system including the near-field probing system, optical fiber Mach–Zehnder interferometer and acousto-optic modulator. The momentum values can be further retrieved by the numerical Fourier transform (FT) of the spatial field distribution. However, it usually takes a long time to get a high momentum-resolution result by this method, because high momentum resolution requires scanning over a large spatial area. Besides, the spectral range of this method is generally limited as it has to use the coherent laser light. Another method to measure the momentum-resolved spectra is

*Corresponding authors

Email addresses: lshi@fudan.edu.cn (Lei Shi),
haiway@ideaoptics.cn (Haiwei Yin), jzi@fudan.edu.cn (Jian Zi)

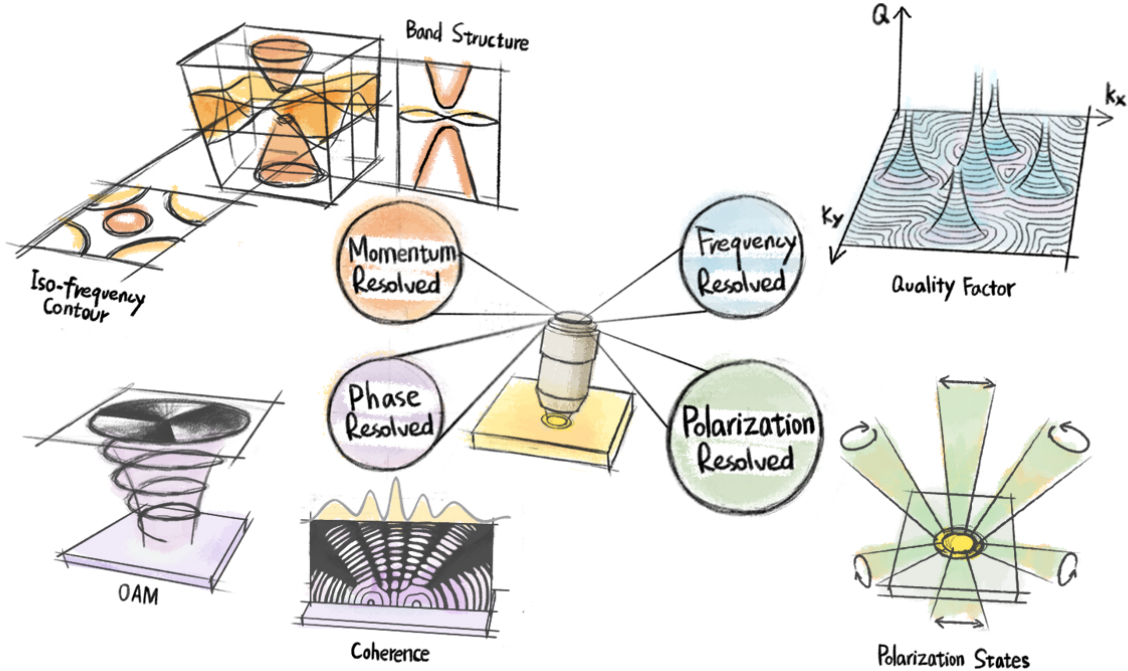


Figure 1: The momentum-space imaging spectroscopy has the capability of momentum-, frequency-, polarization- and phase-resolved measurement. It has been used to study the photonic dispersions including band structures and iso-frequency contours, to extract the key features of eigenmodes like quality factors and polarization states, as well as to characterize the coherence properties and wavefronts of the radiation from nanophotonic materials.

variable-angle spectroscopy [44–46], which can obtain the far-field spectra at different angles with the relative rotation of light source and detector around the sample. The in-plane momentum of photons can be determined by the angle and wavelength values. However, the variable-angle spectroscopy is not suitable for the micro-size samples, because it is usually hard to reduce the sample-plane light spot size down to the micrometer scale. Recently, the optical-FT method [29, 47–53] has been proposed for the study of nanophotonic materials, which is capable of a wide spectral range and high momentum resolution. Instead of numerical FT, this method uses the optical FT performed by optical lenses to obtain the momentum-space information. It doesn't require any one-by-one position scan or angle scan, allowing a fast-speed measurement and the applicability for micro-size samples.

Inspired by the optical-FT momentum-resolved method, the momentum-space imaging spectroscopy (MSIS) system has been developed, which can directly measure the spectral information in momentum space. As illustrated in Fig. 1, the MSIS system has the capability of momentum-, frequency-, polarization- and phase-resolved measurement. It has become a powerful tool for the comprehensive study of nanophotonic materials. Using the aberration-corrected optical system together with the 2D detector, MSIS can capture the photonic dispersions in one shot with high energy and momentum resolution. As different photonic eigenmodes can be easily separated from the momentum-resolved spectrum data, we can further extract other key features of photonic eigenmodes, such as the quality factors [39, 54, 55] and polarization states [53, 56, 57], by use of the post-processing algorithm based on coupled mode

theory. In addition, with the interference configurations, MSIS can obtain not only the intensity but also the phase responses of nanophotonic materials, which is of much help for both fundamental and applied research fields, such as light-matter interaction [30, 58], wavefront control [59–62] and generation of optical vortices based on nanostructures [63, 64]. In the following sections, we first introduce the general principle and experimental set-up of the MSIS system. Then, we focus on its applications including the study of photonic dispersions, photonic eigenmode analyses, the experimental characterization of coherence properties and phase responses and novel light propagation in nanophotonic materials. Both post-processing algorithms and application results are presented.

2. Experimental system design and set-up

2.1. General principle

Momentum space is closely related to real space (position space) by FT. Mathematically, if a function is given in real space, then its FT obtains the function in momentum space [65]. As mentioned above, the momentum information of nanophotonic materials can be retrieved by the numerical FT of the spatial field distribution. However, this method requires the complicated measurement system and is limited in terms of momentum resolution and spectral range.

As illustrated in Fig. 2, the optical lens has an inherent ability to perform 2D optical FT [66, 67], providing an efficient way for the measurement of momentum space information. In Fig. 2, light emanates from a sample which is placed on the front focal plane of the lens, and propagates along the direction

(θ, φ) with the momentum vector $\mathbf{p} = \hbar\mathbf{k}$ (the purple arrow), where \mathbf{k} is the wavevector. The projection of \mathbf{p} onto the sample plane gives the in-plane momentum vector \mathbf{p}_{\parallel} (the orange arrow), which can be determined by (θ, φ)

$$\mathbf{p}_{\parallel} = (k_0 \sin \theta \cos \varphi, k_0 \sin \theta \sin \varphi), \quad (1)$$

where $k_0 = 2\pi/\lambda$ is the magnitude of \mathbf{k} . Through the optical lens, light with momentum \mathbf{p} can be focused on the back focal plane (BFP) of the lens. A position vector \mathbf{r}_{BFP} is defined on the BFP to indicate where the light is focused. In the ideal case where the lens is aberration free and infinity corrected, the Abbe sine condition [68, 69] can be fulfilled, according to which the magnitude of \mathbf{r}_{BFP} is proportional to the sine of θ . Thus, there exists a relationship between (θ, φ) and the position vector \mathbf{r}_{BFP} (the green arrow in Fig. 2), given by

$$\mathbf{r}_{\text{BFP}} = (h \sin \theta \cos \varphi, h \sin \theta \sin \varphi), \quad (2)$$

where h is a factor related to the focal length of lens and the refractive index of environment. It can be clearly seen from Eqs. (1) and (2) that there is a one-to-one correspondence between \mathbf{r}_{BFP} and \mathbf{p}_{\parallel} , indicating that the BFP image can be viewed as the in-plane momentum distribution of light from sample.

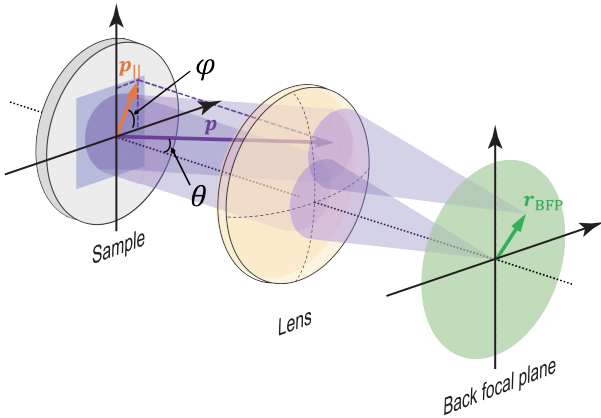


Figure 2: Schematic graph of the 2D optical Fourier transform performed by an optical lens. The projection of light momentum \mathbf{p} (the purple arrow) onto the sample plane gives the in-plane momentum vector \mathbf{p}_{\parallel} (the orange arrow), which can be determined by the light propagation direction (θ, φ) . In the ideal case where the lens is aberration free and infinity corrected, there exists a relationship between (θ, φ) and the position vector \mathbf{r}_{BFP} where the light is focused (the green arrow in Fig. 2) given by Eq. (2).

2.2. Experimental setup

Based on the optical FT performed by optical lenses, the MSIS system has been developed, which is composed of three parts: a momentum-space imaging part, a spectral imaging detection part and a phase-resolved measurement part. The schematic diagram of the MSIS experimental setup is illustrated in Fig. 3. Note that, for simplicity, we only show the reflection configuration here. The MSIS system can also work in both reflection and transmission configurations. In the following part of this article, we will show the experimental results including

both transmission and reflection applications. And more details about the transmission setup can be found in Refs. [57, 64].

The momentum-space imaging part is the optical system used for high-resolution momentum-space imaging. As mentioned above, we can use an optical lens to perform the optical FT and obtain the momentum space information on its BFP. However, a single lens is insufficient to provide high-resolution imaging results due to the optical aberrations [67, 69] such as chromatic aberration, spherical aberration and coma. Aberrations cause the image to be blurred or distorted, greatly affecting the measuring accuracy. Therefore, instead of a single lens, a plan-corrected apochromatic objective lens [70] is used in the MSIS experimental setup, containing a complex internal lens system made up of many lens elements. The objective lens enables the aberration correction, as well as the microscale-sample measurement. Then, we use four achromatic doublet lenses following the objective lens to image its BFP on the detector. The four-lens imaging part is kept in the vicinity of the optical axis so that the paraxial approximation is valid where light is treated as a ray and its wave nature resulting in aberrations is omitted [67].

It is worth mentioning that, the similar optical system to the four-lens imaging part can also be added between the light source and the beam splitter close to the objective. In this case, there is an image plane of the objective's BFP in the incident light path, on which one point corresponds to one angle of light on the sample based on Eq. (2). By focusing light from source on this BFP image plane, we are able to control the incident light angle, which is important for many experiments, such as the grating diffraction experiment and the phase-resolved measurement as described below.

The spectral imaging detection part of MSIS allows us to capture the momentum-space spectral information in one shot, providing a greatly improved measuring efficiency. This part has three operation modes: the iso-frequency mode, the colorful mode and the spectral mode. (1) In the iso-frequency mode, a 2D monochrome charged-coupled-device (CCD) camera is placed on the imaging plane of the BFP of objective lens, as illustrated in Fig. 3. The light frequency of interest can be selected by using a single-wavelength laser source, or an incoherent source in conjunction with a narrow bandpass filter. In this way, the iso-frequency contour [71, 72], which indicates the optical modes with constant frequency value in momentum space, can be imaged on the 2D monochrome CCD camera. It is essential for understanding photonic phenomena dependent on the direction of group velocities, such as negative refraction [73, 74] and superprisms [75]. (2) In the colorful mode, a 2D color CCD camera is used instead of the monochrome one. With the illumination of white light source, the color distribution in momentum space can be directly imaged. Given the close association between momentum space and angular distribution, the colorful mode provides a visual way of measuring angle-dependent spectral responses for nanophotonic materials, especially structural color materials [76–78]. (3) In the spectral mode, the momentum-space information is detected by an imaging spectrometer, with its entrance slit conjugated to the BFP image. Light entering the spectrometer is dispersed by the diffraction

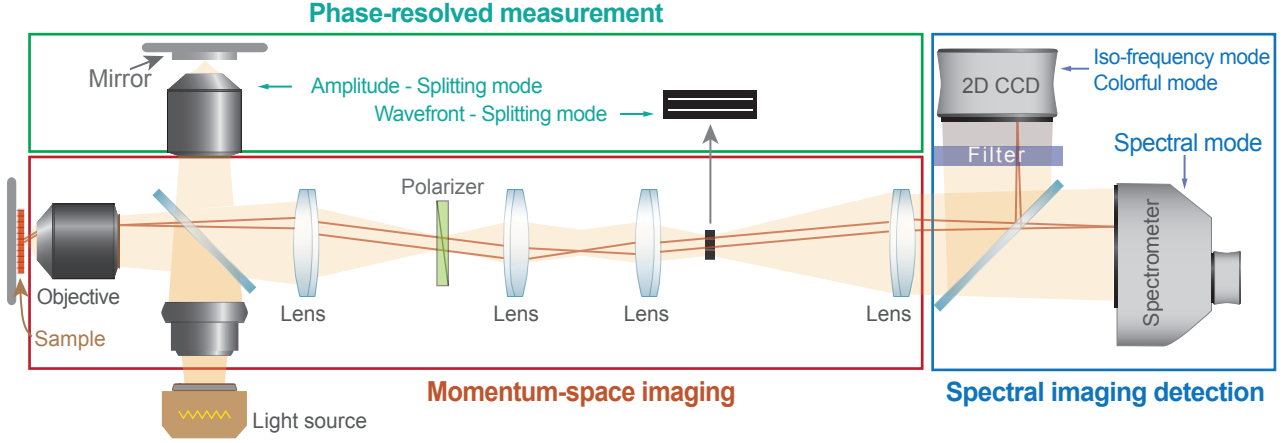


Figure 3: Schematic graph of the momentum-space imaging spectroscopy experimental setup, composed of three parts: momentum-space imaging part, spectral imaging detection part, and phase-resolved measurement part respectively.

grating within, and finally detected by a monochrome 2D CCD camera. One axis of CCD is parallel to the entrance slit and used to resolve the momentum value of light, while the other axis is used to resolve light frequency. In this way, the dispersions along the entrance slit in momentum space can be mapped out at a time. In addition, the imaging spectroscopy can be replaced by a fiber spectrometer, with its optical fiber tip scanning on the BFP image. The fiber spectrometer is more compact and lightweight, but not capable of one-shot imaging measurement.

It is worth mentioning the momentum-space range that can be reached experimentally is determined by the numerical aperture (NA) of the system, and the momentum-space resolution is related to the real-space size detected by the system and the pixels of the CCD detector. In general, a higher momentum-space resolution requires a larger detected real-space size and smaller CCD pixels, which should be considered when designing and building the experimental set-up.

With the phase-resolved measurement part, MSIS can allow us to measure the phase information in addition to the amplitude and frequency distribution. The phase-resolved measurement is realized by the interference configuration including two operation modes: wavefront-splitting mode and amplitude-splitting mode. (1) In the wavefront-splitting mode, the light fields on the sample image plane is split into two separate waves which later go together in momentum space, as illustrated in Fig. 4a. In this mode, a spatial filtering device, generally a double slit, is placed on the image plane of sample. Then, the superposition of radiation fields from different sample areas can be detected and analyzed. If these fields are correlated or coherent with each other, interference patterns will be observed. Through the visibility and position of the interference fringes, we are able to obtain the optical phase information and coherence properties of the sample. (2) In the amplitude-splitting mode, a laser beam is split by a beam splitter into two beams, sample beam and reference beam. As illustrated in Fig. 4b, the sample beam is focused onto the sample while the reference beam is focused onto a reference mirror. Then both beams are reflected back and combined together. From the intensity changes of the su-

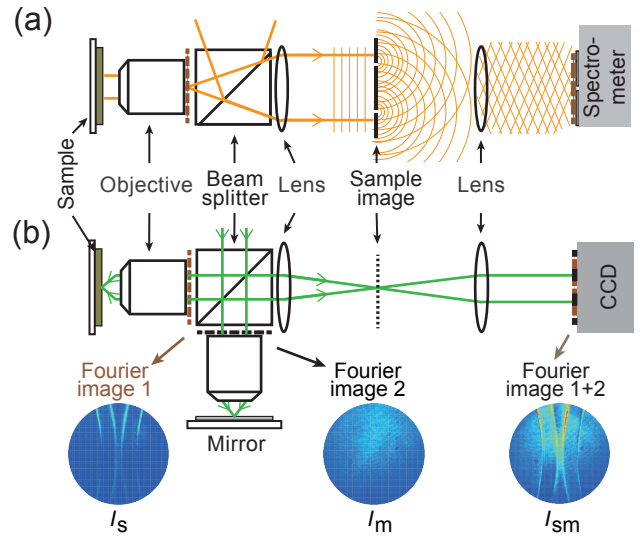


Figure 4: Schematic graph of the phase-resolved measurement configuration: (a) wavefront-splitting mode with a double slit placed on the sample image plane; (b) amplitude-splitting mode, with the typical momentum-space images of reflection from photonic crystal slab sample I_s and from mirror I_m , as well as the superimposed image I_{sm} .

perimposed beam, the phase difference between the sample and the reference mirror can be extracted through two-beam interference analysis. Using the iso-frequency detection mode and phase demodulation methods described below, phase information can be mapped out in parallel over the momentum space.

2.3. System calibration

In this part, we demonstrate the grating diffraction experiment to calibrate the MSIS system and to show the aberration-corrected imaging performance. As illustrated in Fig. 5a, a transmission grating (300 grooves/mm, Thorlabs) is illuminated with white light under the normal incidence. Through the grating, light is diffracted into several beams travelling in different directions. Using the colorful detection mode of the MSIS system, we captured the color diffraction pattern in momentum

space. As can be seen in the lower pannel of Fig. 5b, there is one white spot which is the zero-order beam, and other spots showing a rainbow of colors, that is, non-zero order beams.

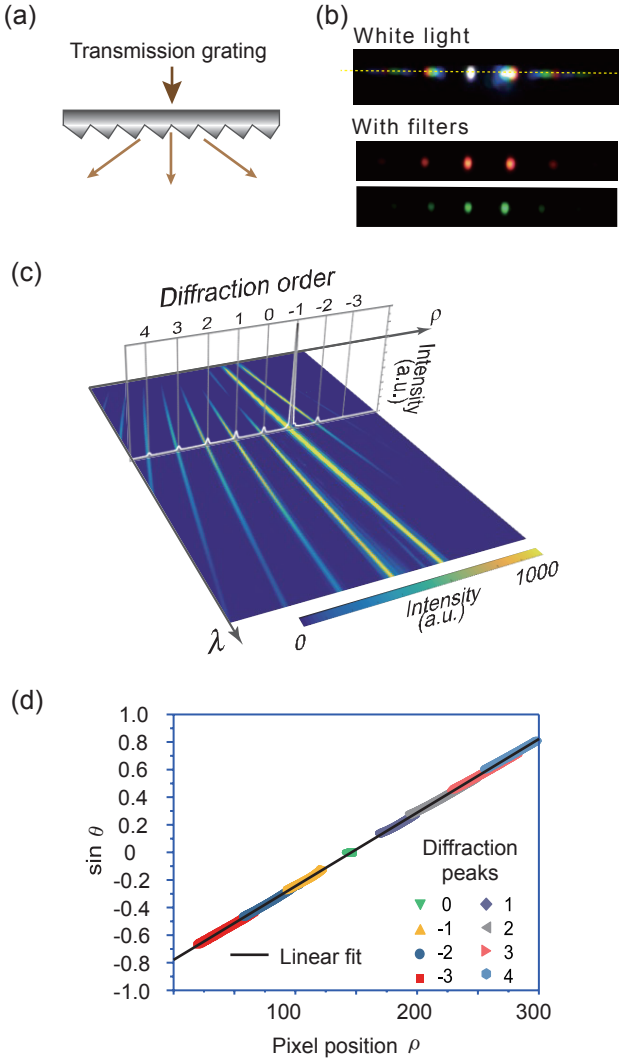


Figure 5: Grating diffraction experiment. (a) Schematic drawing of the transmission grating; (b) experimentally measured color imaging of diffraction pattern in momentum space from the grating under normal incidence; (c) spectral diffraction pattern of the grating obtained the spectral imaging mode; (d) the plot of $\sin \theta$ as a function of detector pixel position ρ extracted from the measured spectral pattern in (c).

For a quantitative analysis, we measured the spectral diffraction patterns along the diffraction direction (yellow dashed line in Fig. 5b) using the spectral detection mode of MSIS. The measured result is shown in Fig. 5c. Theoretically, the position of diffraction peak ρ_{ypeak} corresponds to the angle θ given by the diffraction equation [67]

$$d \sin \theta = m\lambda, \quad (3)$$

where d and m denote the line spacing of grating and diffraction order. It can be concluded from Eqs. (2) and (3) that if the Abbe sine condition is satisfied, ρ_{ypeak} should exhibit linear relationship with $\sin \theta$ as well as λ . As we can see from

Fig. 5c, ρ_{ypeak} indeed vary linearly with λ . For the further verification, we extracted ρ_{ypeak} pixel position and calculated $\sin \theta$ values using Eq. (3). As plotted in Fig. 5d, a good agreement with the linear relation between $\sin \theta$ and ρ_{ypeak} can be clearly observed, indicating that the system achieves good performance in aberration-corrected imaging. Then we can perform a linear polynomial fitting, based on which we are able to calibrate the MSIS system with the relationship between momentum values and detector pixel position ρ .

3. Applications of momentum-space imaging spectroscopy in nanophotonic materials

With the experimental setup demonstrated above, the MSIS system can enable the momentum-resolved and frequency-resolved measurement, including both intensity and phase information. In this section, we demonstrate its applications in nanophotonic materials, including the study of photonic dispersions, photonic eigenmodes, coherence properties and phase information.

3.1. Photonic dispersions

With the capability of high-resolution momentum space measurement, the MSIS system is of great use for the study of photonic dispersions. As mentioned above, photonic dispersions describe the energy levels of photonic eigenmodes in momentum space. Generally, a continuous range of allowed energy levels can be referred to as the energy band, and the range of energy not covered by any band is called the band gap. For the systems with well-defined photonic energy bands, it is common to use photonic band structures as a synonym for photonic dispersions. In this part, we characterize the PBGs and 3D band structures in (ω, k_x, k_y) of nanophotonic materials, to demonstrate the performance of MSIS for photonic dispersion measurement.

3.1.1. Photonic band gap

PBGs [2] are the forbidden energy ranges where no propagating modes exist, which have been used for many applications, including designing special filter, waveguides and resonators. In experiment, PBGs can be clearly revealed from the momentum-resolved spectra measured by MSIS. As an example, we measured a 1D PhC sample. As illustrated in Fig. 6a, the sample is made up of SiO_2 layers with thickness $d_{\text{SiO}_2} = 125$ nm and TiO_2 layers with thickness $d_{\text{TiO}_2} = 85$ nm on the glass substrate, such that the periodicity $a = d_{\text{SiO}_2} + d_{\text{TiO}_2} = 210$ nm.

We first measured its transmission spectrum at $k_{\parallel} = 0$, that is in the normal direction. As shown in the yellow region in Fig. 6b, the transmissivity is almost zero at the wavelength range of 700 to 900 nm, indicating the PBG of the 1D PhC where light is forbidden to propagate inside the sample and thus can be totally reflected. In addition, the zero-transmission caused by PBG is usually angle dependent and polarization dependent. For a further study, we measured the projected dispersion diagrams as the polarized momentum-resolved transmission using the spectral detection mode of MSIS. The polarized measurement is realized by placing a polarizer in the

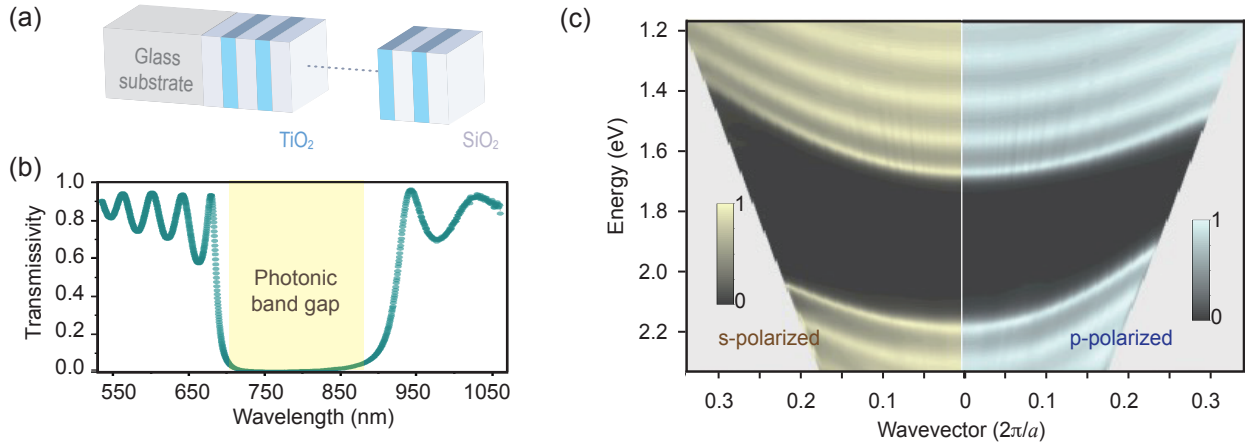


Figure 6: The photonic band gap in the 1D photonic crystal. (a) Schematic drawing of the 1D photonic crystals sample, (b) experimentally measured transmission spectrum at $k_{\parallel} = 0$, (c) experimental $\omega(k)$ dispersion diagram of TE-polarized modes (left side, yellow) and TM-polarized modes (right side, cyan).

momentum-space imaging part of MSIS, as shown in Fig. 3. As the 1D PhC is isotropic in the plane perpendicular to the periodic direction, it is enough to have the dispersion diagrams along one direction. Fig. 6c shows the experimental dispersion diagrams along one direction in the form of transmission. The left side (yellow) shows the s-polarized result indicating TE-polarization modes, and the right side (cyan) shows the p-polarized result indicating TM-polarization modes. The shaded gray areas correspond to the modes out of the NA of the MSIS system. The black region in Fig. 6c where the transmission is almost zero indicates the PBG. It can be seen that the frequency range of PBG shows an wavevector-dependent and polarization-dependent shift, which is in good agreement with the theoretical analysis [2].

3.1.2. 3D band structures in (ω, k_x, k_y)

Unlike 1D PhC, most nanophotonic materials, especially two-dimensional structures, show remarkable anisotropy, requiring the measurement of the photonic dispersions not only along one direction but also across the 2D (k_x, k_y) momentum space. With the ability of 2D optical FT and 2D detection, the MSIS system is capable of measuring the 3D dispersions in (ω, k_x, k_y) space. As an example, we measured the 3D band structures of plasmonic crystal slabs [53] using MSIS. As illustrated in Fig. 7a, the samples studied here are 200-nm-thick silver films coated with 70-nm-thick periodically corrugated polymethyl methacrylate (PMMA) (refractive index of 1.5) layers. The PMMA layers are etched with square (periodicity, 400 nm) and hexagonal (periodicity, 600 nm) array of cylindrical air holes. Due to the periodicity of PMMA array, the propagating surface plasmon polaritons (SPPs) show well-defined band structures [79]. By measuring the photonic dispersions along different directions using the MSIS system, we obtained the full band structures in (ω, k_x, k_y) space of the plasmonic samples. Fig. 7b shows the 3D plot of measured band structures inside the first Brillouin zone (FBZ) at visible wavelength within the NA of the MSIS system.

Specifically, there are two methods to map the 3D band struc-

tures across momentum space. One method is using the spectral detection mode. We first measure the dispersion diagram along one direction in momentum space, which is usually a high symmetry line. Then by rotating the sample in plane relative to the entrance slit of the imaging spectrometer, the entire energy-momentum space could be further mapped out. Fig. 7c plots some examples of dispersion diagrams along different directions. Another method for visualizing band structures is using the iso-frequency detection mode, which enables us to plot the intersection of a constant-energy plane to the dispersion surfaces, namely iso-frequency contour. The 3D band structures can be constructed from a series of iso-frequency contours measured over a continuous range of frequencies. Some examples of measured iso-frequency contours at a few wavelengths are also presented in Fig. 7c.

Note that the results shown here are limited with the radiative modes. Combining with a method of compound lattice [80, 81], the MSIS system can also be used to measure the nonradiative modes below the light cone. The compound lattice introduces the periodic weak scattering which can transfer the nonradiative modes below the light cone to those inside the light cone. More details about this method can be found in Refs. [80, 81].

3.2. Key features of photonic eigenmodes

In addition to the energy-momentum relations, other key features of photonic eigenmodes, such as quality factors and polarization states, also play important roles in nanophotonic material study. The MSIS system can be used to extract these key features with the post-processing algorithm based on the temporal coupled-mode theory (TCMT) [3, 82, 83]. In this part, we demonstrate the extraction of quality factors and polarization states for the plasmonic sample mentioned above. Note that the metallic film in the sample is thick enough to avoid transmission. Thus, only the output channels in reflection are considered here. TCMT can also be applied on the system with transmission where there are more channels, about which more details can be found in Refs. [39, 54, 55, 57, 64, 84].

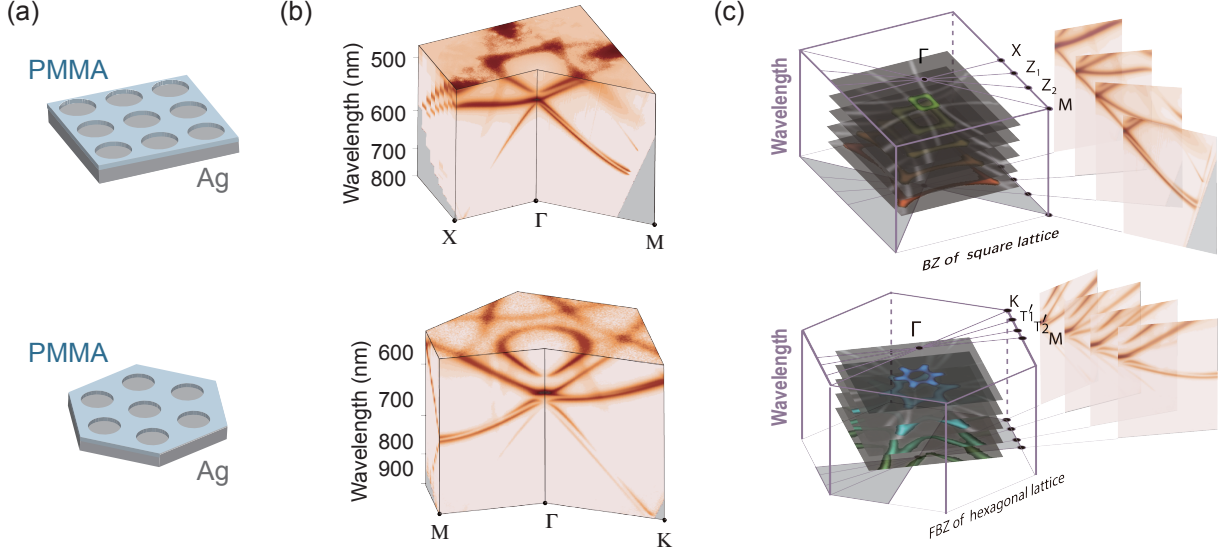


Figure 7: 3D band structure measurement for plasmonic samples. (a) Schematic drawing of the plasmonic crystal samples with square lattice and hexagonal lattice. (b) 3D plot of measured band structures at visible wavelength inside the first Brillouin zone within the numerical aperture of the momentum-space imaging spectroscopy system. (c) Examples of measured projected dispersion diagrams along different directions and iso-frequency contours at a few wavelengths. Parts (b)–(c) are adapted from ref. [53].

3.2.1. Quality factors

Once excited, the photonic eigenmodes can lead to optical resonances which provide an efficient way to channel light to the external environment. To describe the rate at which the resonances dissipate their energy, we use the parameter called quality factor (Q factor), which is a dimensionless quantity describing the decay rate of energy loss relative to the stored energy. A higher Q factor [54, 85, 86] indicates a lower energy dissipation rate, as well as a longer lifetime of the photonic eigenmode. Typically, in a photonic system, there are several channels for a mode to dissipate its energy, for example, the radiative channel to far-field radiation and the non-radiative channel to absorption. We can define the radiative and non-radiative Q factors by [2]

$$Q_r \equiv \frac{\omega_0}{2\gamma_r}, \quad Q_{nr} \equiv \frac{\omega_0}{2\gamma_{nr}} \quad (4)$$

where ω_0 is resonance frequency, γ_r is radiative decay rate and γ_{nr} is non-radiative decay rate. The total Q factor can be then yielded by

$$\frac{1}{Q_{\text{tot}}} = \frac{1}{Q_r} + \frac{1}{Q_{nr}}. \quad (5)$$

To analyze the energy damping properties through different channels, we use the TCMT [3, 82, 83]

$$\frac{dA}{dt} = (-i\Omega - \Gamma_{nr} - \Gamma_r)A + D^T s_+, \quad (6a)$$

$$s_- = C s_+ + DA, \quad (6b)$$

where A is a column vector containing the amplitudes of optical modes and matrix Ω represents resonance frequencies and coupling between these modes. Once excited with the incoming waves s_+ , optical modes couple with the outgoing waves s_- , with the coupling matrix D . Matrix Γ_r describes radiation loss; its diagonal elements $\{\gamma_{j,r}\}_{j=1}^N$ are the radiative decay rates

of the resonances, and its off-diagonal elements couple the resonances via radiation. Matrix Γ_{nr} describes non-radiative decays due to absorption, and it is assumed to be diagonal with $\Gamma_{nr} = \text{diag}(\gamma_{1,nr}, \dots, \gamma_{N,nr})$ here. C is the reflection matrix for the direct (non-resonant) response.

As an example, we have extracted both Q_r and Q_{nr} from the unpolarized momentum-resolved reflection spectra measured by the MSIS system for the square-lattice plasmonic sample demonstrated above. With an unpolarized incident light and with a detector that does not resolve polarization, the measured reflection is polarization averaged and is given by $\text{Tr}(r^\dagger r)/2$, where r is the polarization-resolved reflection matrix including both direct and resonant reflections

$$r = \begin{pmatrix} r_{ss} & r_{sp} \\ r_{ps} & r_{pp} \end{pmatrix}. \quad (7)$$

Through the TCMT, the reflection matrix r at frequency ω is written as [39]

$$r = [I - iD(\omega - \Omega + i\Gamma_r + i\Gamma_{nr})^{-1}D^\dagger]C, \quad (8)$$

where I is a two-by-two identity matrix and $C = \exp[i \text{diag}(\theta_s^{(d)}, \theta_p^{(d)})]$ can be modeled by the reflection matrix of a homogeneous dielectric slab [39, 82] on a silver substrate. Because the metallic film in the sample is thick enough to avoid transmission, the extinction equals one minus reflection, given as

$$\text{Ext} = 1 - \frac{\text{Tr}(r^\dagger r)}{2}. \quad (9)$$

For the purpose of extracting quality factors, the detailed polarization information is not important, and to a good approximation one can treat each resonance as coupling either to the s polarization only or to the p polarization only. Under this

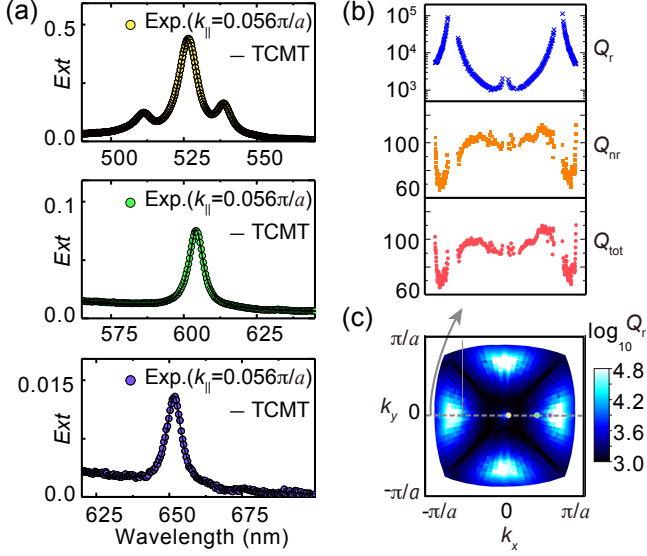


Figure 8: Quality factor analyses for band 2. (a) Experimental extinction spectra (colorful dots) and fitting curves with the temporal coupled-mode theory (black lines) at three different wavevectors along $\Gamma - X$ direction, that is $k_{\parallel} = 0.056 \pi/a$ (yellow dots), $0.40 \pi/a$ (green dots) and $0.56 \pi/a$ (purple dots); (b) distributions of extracted values of Q_r , Q_{nr} and Q_{tot} along $\Gamma - X$ direction; (c) the momentum-space distribution of extracted Q_r inside FBZ above the light cone. Parts (a)–(c) are from Ref. [53].

assumption, inserting Eq. (8) into Eq. (9) yields the extinction spectrum as a function of frequency ω

$$Ext = 1 - \frac{1}{2} \left(\left| \frac{1 - f_s}{1 + f_s} \right|^2 + \left| \frac{1 - f_p}{1 + f_p} \right|^2 \right), \quad (10)$$

where

$$f_s \equiv \sum_{j \in s} \frac{i\gamma_{j,r}}{\omega - \omega_j + i\gamma_{j,nr}}, \quad f_p \equiv \sum_{j \in p} \frac{i\gamma_{j,r}}{\omega - \omega_j + i\gamma_{j,nr}}. \quad (11)$$

$\sum_{j \in s}$ denotes a summation over the resonances that couple to s polarization, and similarly for $\sum_{j \in p}$.

By fitting the experimentally measured extinction spectra to Eq. (10), the radiative and non-radiative decay rate can be extracted, and then the Q factors can be calculated by Eqs. (4) and (5). Fig. 8 shows Q factor analysis results for the lowest band plotted in the upper panel of Fig. 7b (hereinafter referred to as band 2). Some examples of measured extinction spectra (colorful dots) and fitting curves (black lines) are shown in Fig. 8a, from which it can be seen that they are in good agreement. The extracted values of Q_r , Q_{nr} and Q_{tot} along $\Gamma - X$ direction are plotted in Fig. 8b. While both Q_{nr} and Q_{tot} are no more than 120, Q_r can be up to 10^5 and even diverging. The diverging Q_r means the optical mode is decoupled from the free space and is so-called bound state in the continuum (BIC) [54, 87]. As demonstrated above, the MSIS system is capable of measuring spectral information across the 2D (k_x, k_y) momentum space, from which the momentum-space distribution of Q factors can be attained. As shown in Fig. 8c, the momentum-space distribution of radiative Q factors of band 2 has been mapped out, where five BICs are clearly observed.

3.2.2. Polarization states

Another key feature of photonic eigenmodes is their polarization. The polarization state can be characterized by a set of coupling coefficients $D = (d_s, d_p)^T$ which describe the coupling of the mode to s - and p -polarized radiation in the far field. In recent years, there're increasing attentions attracted to the study of polarization state, as it is related to the novel photonic phenomena like BIC [38, 53, 56], and drives the novel applications of nanophotonic materials on polarization engineering and beam shaping including wavefront control and optical vortex generation [57, 64]. Thus, it is needed to extract the polarization states in experiment.

Using the MSIS system, we can measure the polarization-dependent momentum-resolved spectra, from which we can extract the polarization states based on TCMT. As an example, we analyzed the polarization states on band 2 in the upper panel of Fig. 6b [53, 84]. We use unpolarized illumination and place a polarizer to measure the polarization-dependent spectra. The polarizer is oriented facing \hat{z} direction with its transmission axis pointing along $\hat{\alpha}$, with $\hat{\alpha} \cdot \hat{z} = 0$. For light incident along \hat{k} , the polarizer projects the electric field onto an effective transmission axis [53, 88]

$$\hat{t} = \frac{\hat{k} \times (\hat{\alpha} \times \hat{z})}{|\hat{k} \times (\hat{\alpha} \times \hat{z})|}, \quad (12)$$

which is essentially a projection of $\hat{\alpha}$ along the \hat{z} direction onto the \hat{s} - \hat{p} plane. Then the detected \hat{k} -direction flux with a polarizer is $I(\mathbf{E}^+, \hat{k}, \hat{\alpha}) = |\hat{t} \cdot \mathbf{E}^-|^2$ (\mathbf{E}^+ and \mathbf{E}^- are incident and reflected waves). Note that in the case of unpolarized incidence, we need to average over randomly polarized incident fields. Then we can obtain the relationship between the polarization-dependent extinction Ext and reflection matrix r

$$Ext(\hat{k}, \hat{\alpha}) = 1 - \left\| \hat{t} \cdot \hat{s}, \hat{t} \cdot \hat{p} \right\|^2 r. \quad (13)$$

Assuming only one resonance contributes within the frequency range of interest and inserting Eq. (8) into Eq. (13), we get

$$Ext(\hat{k}, \hat{\alpha}) = \frac{2\gamma_{nr} |\hat{t} \cdot \vec{d}|^2}{(\omega - \omega_0)^2 + (\gamma_r + \gamma_{nr})^2}, \quad (14)$$

where $\vec{d} = d_s \hat{s} + d_p \hat{p}$ and \hat{t} is defined in Eq. (12). When the polarizer angle $\hat{\alpha}$ is at $0^\circ, 45^\circ, 90^\circ$ relative to \hat{k}_{\parallel} , we have $\hat{\alpha} = \hat{k}_{\parallel}, (\hat{k}_{\parallel} - \hat{s})/\sqrt{2}, \hat{s}$, respectively, and the effective transmission axis \hat{t} is $\hat{p}, [(\hat{k}_{\parallel} - \hat{s}) \cos \theta - \hat{z} \sin \theta]/[\sqrt{1 + \cos^2 \theta}], \hat{s}$, respectively. From Eq. (14), we get

$$\frac{Ext_{0^\circ}}{|d_p|^2} = \frac{Ext_{45^\circ}}{|d_p - d_s \cos \theta|^2 / (1 + \cos^2 \theta)} = \frac{Ext_{90^\circ}}{|d_s|^2}, \quad (15)$$

where $\theta = \arccos(\hat{k} \cdot \hat{z}) \in [0, \pi/2]$ is the reflected (or incident) angle. Solving Eq. (15) yields

$$\frac{|d_s|^2}{|d_p|^2} = \frac{Ext_{90^\circ}}{Ext_{0^\circ}}, \quad (16)$$

$$\cos \theta_{sp} = \frac{\Re(d_s^* d_p)}{|d_s d_p|} = \frac{Ext_{0^\circ} + Ext_{90^\circ} \cos^2 \theta - Ext_{45^\circ} (1 + \cos^2 \theta)}{2 \cos \theta \sqrt{Ext_{0^\circ} Ext_{90^\circ}}}, \quad (17)$$

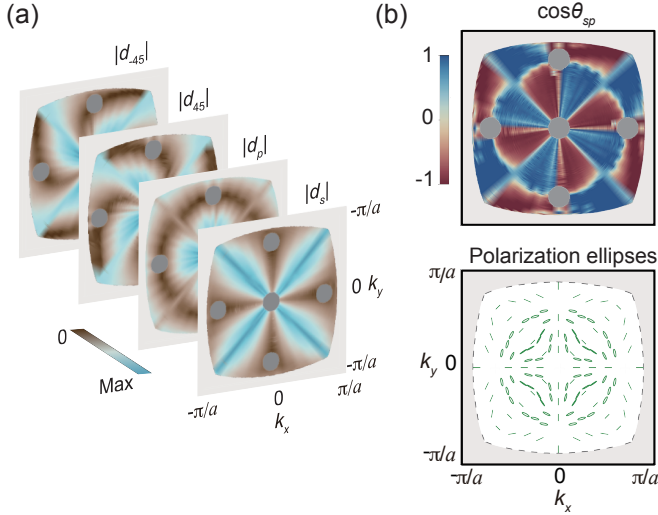


Figure 9: Polarization state analyses for band 2. (a) the measured amplitudes of coupling coefficients for s -, p - and $\pm 45^\circ$ components, (b) the distribution of phase difference $\cos \theta_{sp}$ between s and p components (upper panel) and measured polarization ellipses (lower panel). Parts (a)–(b) are adapted from Ref. [53].

where we define $\theta_{sp} \equiv \arg(d_s/d_p)$ as the phase difference between s and p components. When $\cos \theta_{sp} = 0$, it corresponds to the linear polarization. For the case where $\cos \theta_{sp}$ is not zero, we can use the circularly polarized incident light to further resolve whether it is left-handed (LH) or right-handed (RH). The mode with the LH polarization state can give a stronger response to the LH incidence, and vice versa. In experiment, a waveplate can be added to generate the circularly polarized incidence. Based on the responses under the LH and RH incidences, the polarization states can be fully resolved.

The results for band 2 are shown in Fig. 9. In Fig. 9a, we plot the distribution of $|d_s|$, $|d_p|$, $|d_{45}|$ and $|d_{-45}|$ inside FBZ, which can be derived from Eqs. (15) and (16). Then the phase differences $\cos \theta$, determining the deviation from linear polarization, can be yielded by Eq. (17). In Fig. 9b, the momentum-space distribution of $\cos \theta$ (upper panel) and polarization ellipses (lower panel) have been plotted. Five polarization vortices are observed, which have been proved to be the topological nature of BICs mentioned above [38, 53, 56].

Note that we can not only extract the polarization states of photonic eigenmodes, but also analyze the polarization responses of the sample which is important for the polarization conversion and beam shaping. More details about the polarization response analyses can be found in Refs. [57, 64].

3.3. Coherence properties and phase information

With the phase-resolved measurement part, MSIS can also allow us to measure the phase information in addition to the intensity distribution. Here, we demonstrate its applications in the study of the coherent fluorescence emission of hybrid photonic-plasmonic crystals [58], optical phase shifting caused by SPP modes and guided resonance modes.

3.3.1. Coherence properties

Coherence properties [67, 89] are generally divided into two kinds: temporal and spatial coherence property. They describe correlations between electric fields at different times and locations respectively, which are in close association with many features of nanophotonic materials, like frequency selectivity [24, 90] and directionality effect [58]. The MSIS system, we can obtain both temporal and spatial coherence properties.

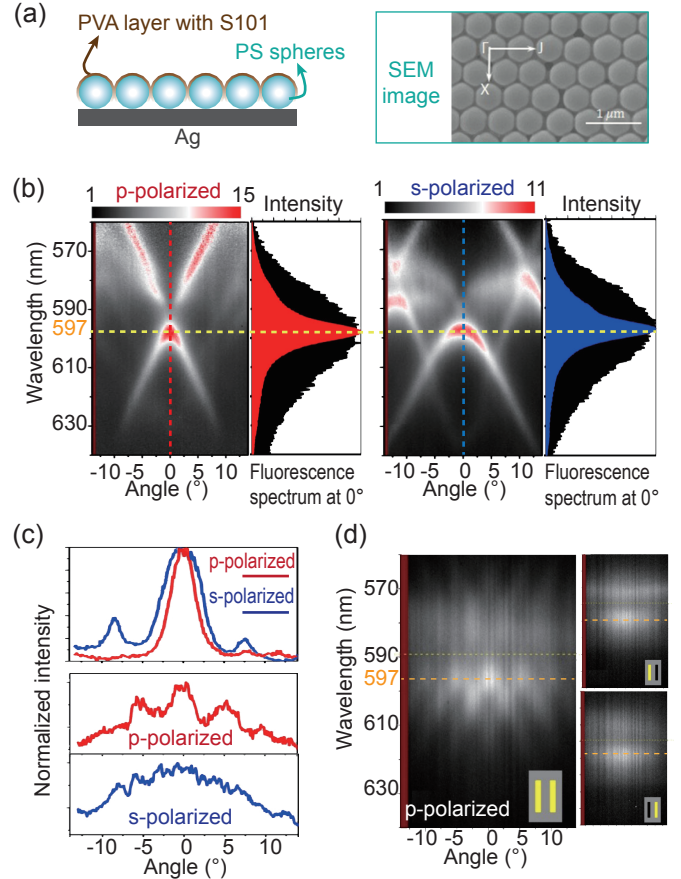


Figure 10: Coherence property analyses for the hybrid nanophotonic material. (a) Schematic drawing of the hybrid photonic-plasmonic crystal sample and scanning electron microscope (SEM) image; (b) experimental angle-resolved fluorescence emission spectra of p - (left, red) and s - (right, blue) polarization along $\Gamma - J$ direction, with the spectra at 0° plotted on the right side; (c) the plot of emission intensity as a function of emission angle around 597 nm without (upper panel) and with (lower panel) double-slit; (d) angle-resolved p -polarized emission spectra of the sample with double-slit (left) and single-slit (right). Parts (a)–(d) are from Ref. [58].

Here, we used a hybrid photonic-plasmonic crystal sample as an example [58]. As shown in Fig. 10a, the sample is composed of monolayer array of polystyrene (PS) spheres with 500-nm diameter on the 200-nm thick Ag thin film, covered with a nominal 50-nm thick fluorescent-molecular (S101)-doped polyvinyl alcohol (PVA) layer. This hybrid nanophotonic material supports photonic eigenmodes characterized by complex photonic dispersions. Fig. 10b shows the measured angle-resolved fluorescence emission spectra of p - (left) and s - (right) polarization along $\Gamma - J$ direction, where enhanced fluorescence emission is observed along the dispersion.

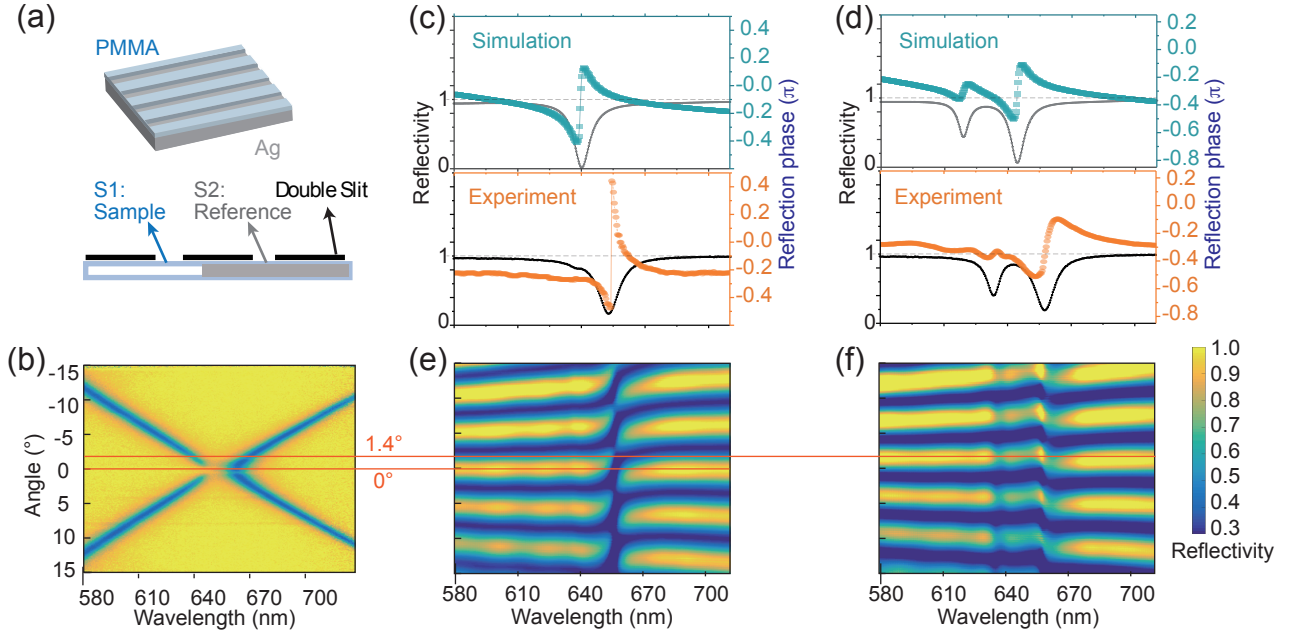


Figure 11: Angle-dependent phase shifting effect caused by SPP modes. (a) Schematic drawing of the plasmonic crystal sample with ribbon array (upper panel) and the placement of double slit (lower panel); (b) experimental dispersion diagram along $\Gamma - X$ direction; (c)(d) the simulated (upper panel) and experimental (lower panel) results of reflectivity and reflection phase distribution in spectrum space under the incidence of (c) 0° and (d) 1.4° ; (e)(f) experimental angle-resolved spectra with double-slit under the incidence of 0° (left) and 1.4° (right).

We firstly studied the temporal coherence property for the optical-mode modified fluorescence emission. Based on the coherence theory [89], the degree of temporal coherence is related to the spectral linewidth of emission light, indicating how monochromatic a light source is. As plotted in Fig. 10b on the right side of the angle-resolved spectra, the fluorescence emission spectra at zero emission angle (along red and blue dashed lines) were selected. The red and blue parts are emission with the photonic-plasmonic structure, while the black ones are the emission without structure (just flat S101-doped PVA layer with the same thickness on top of the silver surface). It is clear that the fluorescence emission without structure (black ones with 37 nm bandwidth) is broader than that with structure (colored ones with 9 nm bandwidth). Calculating the coherence time by one over the spectral width in units of frequency, it is indicated that the quasi-two-dimensional hybrid photonic-plasmonic crystal material has produced around 4-time increase of coherence time for the fluorescence emission. Like the relationship between temporal coherence and frequency spectral linewidth, the spatial coherence is strongly related to the bandwidth of wavevector spectrum. To experimentally investigate it, the emission intensity as a function of the emission angle (along the yellow dashed line in Fig. 10b) at 597 nm, the center wavelength of the optical mode around Γ point, has been plotted and shown in the upper panel of Fig. 10c. The full width at half-maximum for p -polarization (red) is smaller than that for s -polarization (blue), indicating a larger mode volume in sample space that p -polarized emission has.

The wavefront splitting interference configuration has been used for a further study on the spatial coherence property. Fig. 10d shows the angle-resolved p -polarized emission spectra

of the sample with double-slit (left), as well as that with single-slit of the same slit width (right). The double-slit used here has a equivalent slit separation of $7 \mu\text{m}$ on sample plane, as well as a slit width of $2 \mu\text{m}$. It can be seen that clear interference fringes can be observed with double-slit, while no fringes have been observed with single-slit. This is a direct evidence of a long-range spatial coherence of the emission field on sample plane. For different polarization cases, we measured the angle-dependent intensity distributions for p - and s - polarization at 597 nm, as plotted in the lower panel of Fig. 10c. The interference fringe from p -polarization emission is clear while from s -polarization emission nearly no fringes can be observed. It indicates a longer coherence length for p -polarized emission, which is in agreement with the result obtained above. Based on the double-slit size parameters, the interference fringe peaks are expected to be at about ± 5 degree, in a good agreement with the experimental interference results in Fig. 10c, d. Note that there're small vertical fringes in Fig. 10d which are much denser than the interference fringes. They came from the noise signals on the images.

3.3.2. Phase responses

Due to the wave nature of light, it is common to use complex coefficients to describe differences between incident and emergent light for optical materials [67, 91]. For example, complex reflection coefficient is defined as the ratio of complex amplitudes of reflected wave \mathbf{E}_r to that of incident wave \mathbf{E}_i , given as

$$\mathbf{R}_c = \frac{\mathbf{E}_r}{\mathbf{E}_i} = R_c e^{i\phi}, \quad (18)$$

whose squared modulus $|R_c|^2$ gives the reflectivity and complex phase ϕ is associated with optical phase change upon reflection. Notably, R_c is in general dependent on the angle and polarization. Therefore the reflection coefficient $R_{\sigma\mu}^\theta$ of μ -polarized incident wave reflected into a σ -polarized wave along θ direction is more in use [92]. The analyses of angle-dependent and wavelength-dependent reflection coefficient $R_{\sigma\mu}^\theta$, especially its phase factor, play an important role in the study of light modulation using nanophotonic materials, including metalems [61, 62, 93] and polarization conversion [64, 92, 94]. For that reason, it is important to measure the phase information in an angle-resolved, that is momentum-resolved, manner. In this part, we demonstrate the phase measurement performed by the MSIS system using wave-splitting and amplitude-splitting configurations respectively.

We can use the wave-splitting configuration to measure the phase distribution in spectrum space. As an example, we measured a plasmonic sample, which is the 200-nm-thick silver substrate coated with PMMA ribbon array (periodicity, 550 nm; PMMA thickness, 70 nm), as illustrated in, the upper panel of Fig. 11a. The angle-resolved reflection spectra along $\Gamma - X$ direction have been experimentally measured and plotted in Fig. 11b, where reflection dips resulted from the excitations of SPP modes are observed. It is known that not only the intensity but also phase can be modulated by the optical modes [95, 96]. In the upper panel of Fig. 11c and d, we plot simulated reflection spectra (black line) and phase distribution (cyan cube) at 0° and 1.4° , calculated using the finite-difference-time-domain method. Phase shifts are observed at the wavelengths of reflection deeps, indicating the angle-dependent and wavelength-dependent phase modulation by SPP modes.

Then we used the wave-splitting interference mode and spectral detection mode of MSIS to measure the angle-dependent and wavelength-dependent reflection phase. As illustrated in the lower panel of Fig. 11a, a double-slit is placed on the image plane of sample. One slit was located on the ribbon-array area, while the other was on the reference area (the flat PMMA layer with no structures). The reflected fields from the two selected areas can be superimposed in the momentum space. Here, the supercontinuum laser is used as the incident light, so that these fields are coherent with each other and interference patterns can be observed by the detected spectrometer. The phase difference between sample and reference areas $\Delta\phi_{rs}$ can be extracted from the position of interference fringes. Specifically, to measure the phase distribution at 0° , the incident light is limited in the normal direction. The experimental angle-resolved spectra are plotted in Fig. 11e, where a fringe shift is observed near 655 nm, corresponding to the reflection deep in Fig. 11b. The exact phase value can also be extracted. At a wavelength of λ , constructive interference occurs where

$$\frac{d \sin \theta}{\lambda} + \Delta\phi_{rs} = 2\pi n. \quad (19)$$

Here n denotes the interference order. d is the equivalent double-slit separation on the sample plane and $\Delta\phi_{rs}$ is the phase difference between sample and reference areas. From Eq. (19),

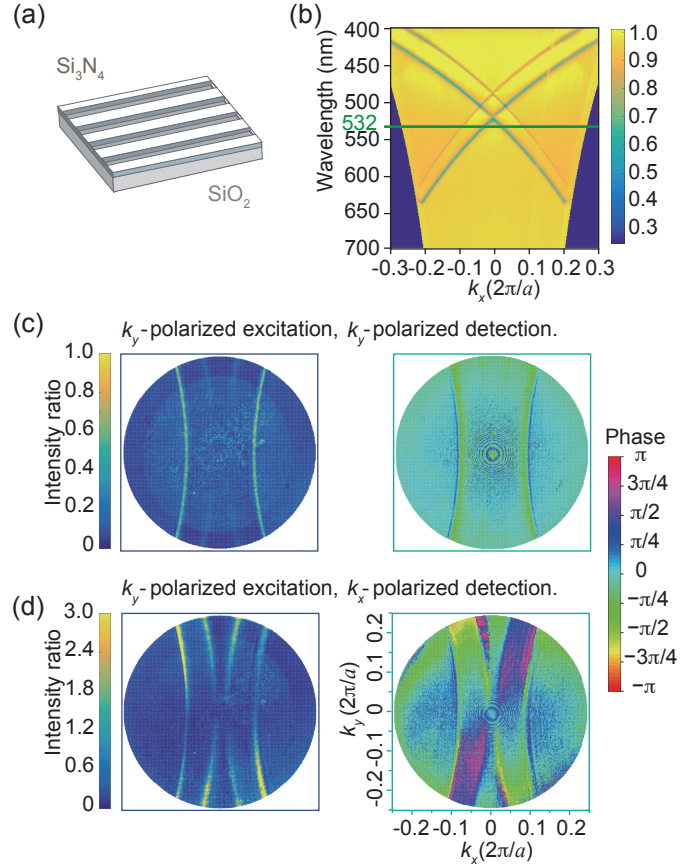


Figure 12: Reflection phase of the photonic crystal slab sample at 532 nm. (a) Schematic drawing of the photonic crystal slab sample with ribbon array; (b) experimental dispersion diagram along $\Gamma - X$ direction; (c), (d) the measured intensity ratio I_s/I_m (left panel) and reflection phase (right panel) distribution in momentum space, with the same polarization of excitation along k_y and different polarization of detection along k_y (c) and k_x (d).

we can get

$$d = \frac{2\pi\lambda}{\sin \theta_n - \sin \theta_{n-1}}, \quad (20)$$

where $\sin \theta_n$ and $\sin \theta_{n-1}$ represent the angles of constructive interference at order n and $n + 1$. Then $\Delta\phi_{rs}$ can be given as

$$\Delta\phi_{rs} = 2\pi n - \frac{d \sin \theta_n}{\lambda}. \quad (21)$$

The extracted $\Delta\phi_{rs}$ distribution in spectrum space is plotted in the lower panel of Fig. 11c as the orange circles, in agreement with the simulation results shown in the upper panel. Besides, changing the angle of incident light, the phase response in the oblique direction has also been analyzed. Fig. 11f shows the experimental angle-resolved spectra under the incidence of 1.4° . Two shifts of interference fringes are observed at around 635 and 660 nm. The extracted reflection phase distribution is shown in the lower panel of Fig. 11d, which agrees with the simulation results shown in the upper panel.

We can also use the amplitude-splitting interference mode and isofrequency detection mode to capture the phase distribution over the 2D momentum space. As an example, we measured the phase response with different polarization in momen-

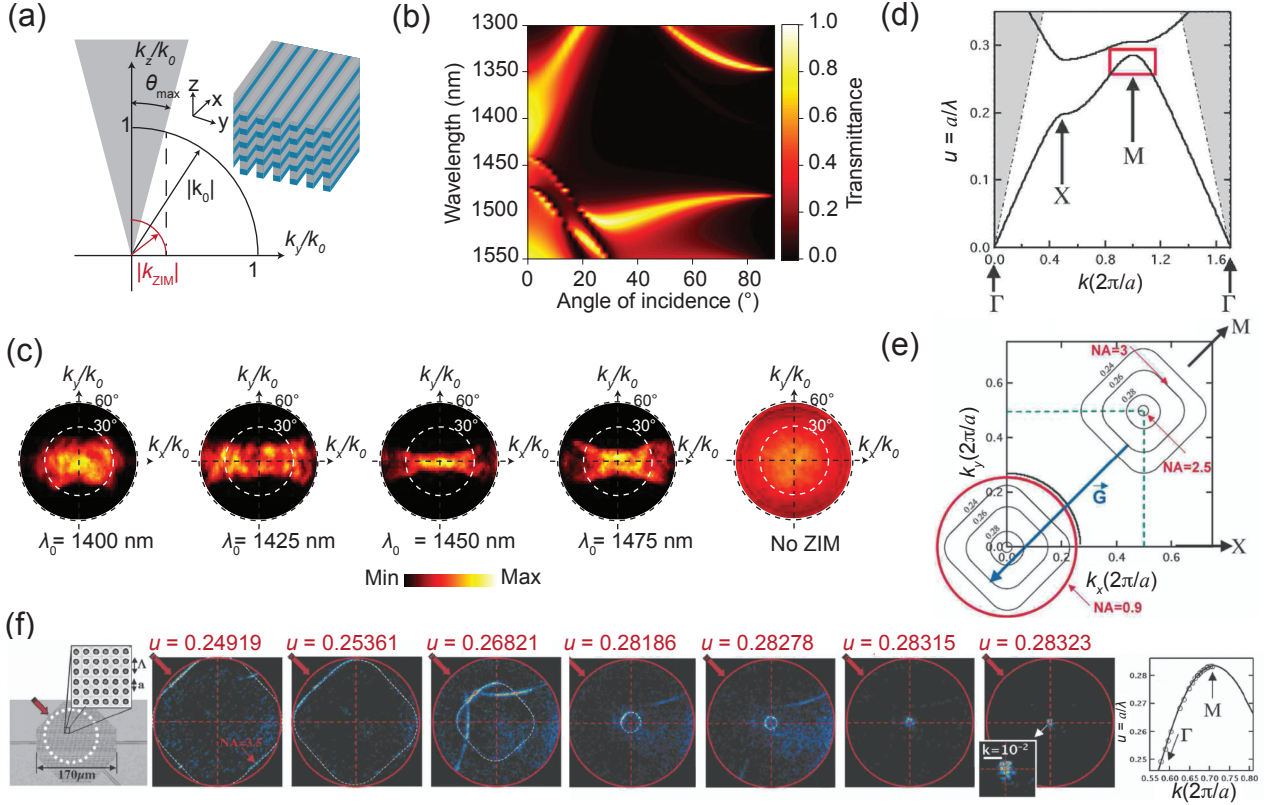


Figure 13: The applications of the omentum-space imaging spectroscopy in the study of zero-index metamaterials (a)–(c) [14] and the self-collimation and localization effect near the photonic band edge (d)–(f) [80]. (a) Iso-frequency contours of air and a low-index metamaterial, illustrating angularly selective transmission due to conservation of the wave vector parallel to the surface; (b) Simulated dispersions of the zero-index metamaterials; (c) Momentum-space images of a beam passing through the fabricated zero-index metamaterial within the low-index band: angularly selective transmission can be observed in the y -direction due to the low effective index, and the last image shows the illumination beam which is uniform intensity over the measured angular range. (d) The energy band diagram where the red rectangle at the M point highlights the region of interest and the shaded region shows the light cone; (e) Collection of the information via the folding of the iso-frequency contours into the light cone; (f) The scanning electron micrograph of the sample and the momentum-space images near the first band edge for increasing reduced energy where the red arrow indicates the direction of the light excitation and the dashed white contours are theoretical iso-frequency contours; the last figure shows the experimental and theoretical dispersion band diagram. [14], Copyright © 2013, Springer Nature. Parts (d)–(f) are from Ref. [80], Copyright © 2009 American Physical Society.

tum spacet of a PhC slab. The sample is a ribbon array of SiN structure ($n_{\text{SiN}} = 2.0$, thickness 100 nm, periodicity $a = 360$ nm) on the SiO₂ substrate, as illustrated in Fig. 12a. The guided resonance modes in PhC slabs can significantly affect their optical responses of externally incident light, in terms of both intensity and phase. The dispersion diagram along $\Gamma - X$ direction, in the form of transmission, has been measured and plotted in Fig. 12b.

For the phase measurement, we used a 532-nm laser beam as the light source and introduce polarizers before beam splitter and CCD camera in order to control the polarization of both excitation and detection. We firstly studied the reflection with the polarization of excitation and detection along k_y . The reflection-intensity distributions in momentum space from sample (I_s) and reference mirror (I_m) have been measured separately. The ratio of I_s and I_m are plotted in the left panel of Fig. 12c, from which four resonance strips can be observed. Two of them with larger $|k_y|$ are clearly evident, while the other two are barely perceptible, which indicates different polarization states of these optical modes. To obtain the phase informa-

tion, we then measured the superimposed intensity I_{sm} reflected from sample and mirror. The cosine value of the phase difference between them can be yielded by

$$\cos \phi_{\text{sm}} = \frac{I_{\text{sm}} - (I_s + I_m)}{2 \sqrt{I_s I_m}}. \quad (22)$$

To further extract the ϕ_{sm} value, we can use two methods. One method is using the acousto-optic modulator or the piezoelectric stage to introduce the temporal phase modulation. Then the phase value can be obtained by the phase shifting algorithms [97] such as the Carré algorithm [98]. Another method is tilting the reference beam to introduce spatial phase shifting with fringe patterns in detection plane. Then we can use spatial phase demodulation methods like FT method [64, 99] to extract phase values.

The extracted reflection-phase distribution in momentum space is plotted in the right panel of Fig. 12c, from which the remarkable phase shifts can be observed near the guided resonance modes. By rotating the polarizer before CCD camera, the polarization of detection was adjusted to be along k_x , perpendicular to the polarization of excitation. Then we measured the

reflection intensity from sample and mirror separately, and plotted intensity ratio I_s/I_m distribution in the left panel of Fig. 12d, where all the four resonance stripes can be obviously observed. The high intensity ratio values on resonances indicate the polarization conversion caused by guided resonance modes. We then extracted reflection phase values from Eq. (22), and plotted the phase distribution in the right panel of Fig. 12d, which shows greater reflection-phase changes compared to Fig. 12c.

3.4. More novel light propagation effects in nanophotonic materials

Nanophotonic materials offer unprecedented flexibility for manipulating the light propagation and have distinct physical properties, such as the ability to access near-zero [14, 100–102] or negative refractive index [73, 74, 103], self-collimation [104–107] and light localization [80, 108]. In this section, we review the recent works of using MSIS technique to exhibit novel light propagation effects in nanophotonic materials including metamaterials and photonic structures.

As an example, Fig. 13a–c shows the application of momentum-space imaging in the study of zero-index metamaterials by Moitra et al. [14]. The zero-index metamaterial here consists of 200- μm -long silicon rods that support electric and magnetic resonances, and are separated by a low-index material — silicon dioxide. As illustrated with the iso-frequency contours depicted in Fig. 13a, the wave vector is restricted to extremely small values in a low-index metamaterial. As a result, light incident at high angles with $k_{y,0} > |k_{\text{ZIM}}$ is reflected while near-normal incident light $k_{y,0} < |k_{\text{ZIM}}$ is transmitted. This effect is evident in the simulated transmission dispersion diagrams as shown in Fig. 13b, indicating the material exhibits near-zero index. To prove it experimentally, the sample was illuminated by the incident light with angles upto 58.2°. The experimental momentum-space imaging result is shown in Fig. 13c. Within the low-index region between 1400 and 1475 nm, tighter confinement of k_y is observed with progressive lowering of the refractive index, in agreement with the simulated data.

In addition to the effect of near-zero refractive index, Thomas et al. have used the momentum-space imaging to investigate the self-collimation and localization effect near the photonic band edge, as shown in Fig. 13d–f [80]. To measure the iso-frequency contours near the boundaries of the FBZ, a properly designed 2D probe grating was used to provide the reciprocal vectors \vec{G} to transfer the dispersion below light cone into the far field, as illustrated in Fig. 13e. The measured momentum-space images are shown in Fig. 13f. It can be seen that the iso-frequency contours are almost squares in the frequency range of $u = a/\lambda < 0.28$, indicating the self-collimation effect where the light propagates without diffraction. When approaching the band edge, the iso-frequency contours become more homogeneous, evolving toward circles with decreasing radii. At the band edge where $u = 0.28323$, the iso-frequency contour turns into a spot with a wider spread than the linewidth of iso-frequency contours in the self-collimation regime. The linewidth broadening in momentum space indicates the transition from extended to localized modes, which is related to the

theoretically lower group velocity in the upper part of the 2D band shown in the last figure of Fig. 13f.

3.5. Structural color

In this section, we demonstrate the ability of MSIS to visualize the iridescence effect for structural color materials, to demonstrate its potential application in nanophotonic products.

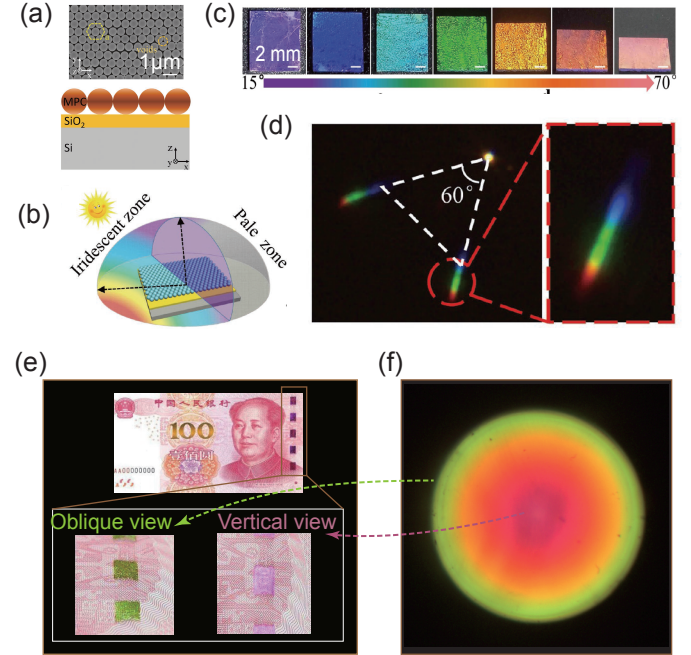


Figure 14: Directly color imaging in momentum space. The composite structure combining 2D photonic crystal and Fabry-Perot cavity: (a) scanning electron microscope image and schematic drawing of the sample, (b) schematic graph of the Janus optical effect, (c) optical photos of different colors brought by the sample when incident under around 25°, (d) the color imaging in momentum space of the composite structure under 25° incident where red rectangle is an enlarged diffraction spot. The anti-counterfeit labels: (e) upper panel: the image of an 100-Yuan banknote, lower panel: optical photos of the anti-counterfeit labels from a vertical view and oblique view; (f) the color distribution in momentum space. Parts (a)–(d) are from Ref. [109], Copyright 2018 WILEY-VCH Verlag GmbH & Co. KGaA, Weinheim.

We first show the result of a composite structure combining 2D colloidal crystal and Fabry-Perot cavity, which can produce high saturated coloration [109]. The sample is composed of polymer-spheres (diameter: 300 nm) monolayer on the silicon wafer with a 270-nm-thick SiO₂ layer, as shown in Fig. 14a. The SEM image in the upper panel clearly shows that polymer-spheres are hexagonal closely packed. The composite structure performs structural color as illustrated in Fig. 14b. In the iridescent zone, the diffuse light produces high-contrast color flicker. With the incident angle of 25°, Fig. 14c displays optical photos of the sample from different view angle. As the view angle increases from around 15° to 70°, it shows different metallic colors from purple to pink. While these photos required multiple shots, the MSIS is capable of showing the iridescence effect in one shot. Using the colorful detection mode, the color imaging of momentum space was recorded for the sample when the incident angle is 25°, and presented in Fig. 14d. It clearly shows

that the reflection spot is white while the diffraction spots are colorful, which provides a visual presentation of the structural color response of the composite structure. In addition, the three spots form an equal-lateral triangle reflecting the hexagonally packed structure of polymer-spheres.

Then we measured a structural-color sample in daily life, an 100-Yuan banknote as shown in Fig. 14e. The anti-counterfeit labels are lined up at the right side, with an obvious angle-dependent structural colors. As shown in the lower panel of Fig. 14e, from a vertical view they perform a pink color, while a green color is performed from an oblique view. Under the incidence of converging white light, the reflection from an anti-counterfeit label has been studied using the colorful detection mode of the MSIS system. As shown in Fig. 14f, the color changes from red at the center gradually to green on the perimeter in momentum space, in good agreement with the lower panel of Fig. 14e. Additionally, the color distribution is isotropic, different from Fig. 14d, which indicates that there is no pale zone and from each direction the anti-counterfeit labels on the banknote always show the iridescent effect.

4. Summary and prospects

Based on the optical FT, the MSIS system can provide efficient ways to detect the frequency distribution in momentum space. In this review, we have described the working mechanism and principles of the MSIS technique and presented its applications in the study of nanophotonic materials. The aberration-corrected setup equipped with 2D detectors enables the MSIS system to capture the high-resolution photonic dispersions at one shot. Using post-processing algorithms based on the coupled mode theory, the key features of photonic eigenmodes, such as quality factors and polarization states, can be extracted from the experimental data measured by the MSIS system. It has played a key role for the study of novel photonic phenomena like BIC, as well as the applications of nanophotonic materials on polarization engineering. Using the interference configurations, the MSIS system can be used to study the coherence properties and phase responses of nanophotonic materials, which is important for both fundamental and applied researches. Furthermore, the MSIS technique has become a powerful tool to characterize and understand the novel light propagation effects in nanophotonic materials, including the near-zero refractive index, self-collimation and light localization. Moreover, the colorful detection mode of the MSIS can directly visualize the iridescent effect in momentum space, showing great potential for practical applications.

Looking forward, there remains substantial scope to improve the capabilities of the MSIS technique. The MSIS technique has been successfully used to study PBGs and more complex band structures in (ω, k_x, k_y) space. However, it is still a great challenge to map the photonic bands in 3D momentum space (k_x, k_y, k_z) . While (k_x, k_y) can be retrieved owing to the conservation of the surface-parallel component of momentum, the surface-perpendicular component k_z cannot be directly measurable as it is distorted and no longer conserved.

Similarly, in electronic systems, k_z is also not conserved because the surface of the material necessarily breaks the translational symmetry in this direction and introduces the inner potential V_0 [110]. Thankfully, V_0 can be determined from photon-energy-dependent measurements by fitting the experimental periodicity along the k_z direction [111, 112]. Using the angle-resolved photoemission spectroscopy (ARPES) [110], k_z can still be extracted with a nearly free-electron approximation for the final states which is a reasonable approximation for a sufficiently high photon energy [111, 113]. In comparison, the surface effects in nanophotonic systems are more complicated. It is hard to directly access to the bulk band structures using such a well-defined parameter as V_0 and relation as the free-electron approximation. It is very worthy of further study to explore a way for mapping the photonic bands in (k_x, k_y, k_z) space.

So far, the applications that we have discussed are primarily focused on characterizing the novel properties and effects in nanophotonic materials. With the rapid development of nanotechnology and nanomaterials, there are other important scenarios demanding more accurate and precise measurements, such as the metrological analysis. To this end, the MSIS system components like mirrors and lenses should be carefully selected in terms of the working wavelength and phase or polarization responses to satisfy the particular measurement need. Furthermore, for the metrological measurement, one of the most important property is its traceability [114]. It is worth being further investigated to establish the traceability of the MSIS system from the establishment of an unbroken chain of calibrations to the standard reference materials.

Conflict of interest

Songting Hu, Guopeng Lu, Ang Chen, Jing Cui, Weiyi Zhang and Haiwei Yin have financial interest in Ideaoptics Instruments Co., Ltd. The remaining authors declare that they have no conflict of interest.

Acknowledgments

We thank Prof. Ling Lu for helpful discussions. The work was supported by the National Key Basic Research Program of China (2016YFA0301103, 2016YFA0302000 and 2018YFA0306201) and the National Natural Science Foundation of China (11774063, 11727811, 91750102 and 91963212). L.S. was further supported by the Science and Technology Commission of Shanghai Municipality (19XD1434600, 2019SHZDZX01 and 19DZ2253000).

Author contributions

Yiwen Zhang, Maoxiong Zhao, Songting Hu, Guopeng Lu and Lei Shi constructed the measurement system. Yiwen Zhang, Maoxiong Zhao, Jiajun Wang, Wenzhe Liu, Bo Wang, Ang Chen and Lei Shi performed the experiment. Yiwen Zhang, Wenzhe Liu, Ang Chen, Lei Shi analysed the data. Wenzhe Liu and Chia Wei Hsu developed the theory models.

Lei Shi, Haiwei Yin and Jian Zi supervised the research. All authors discussed and interpreted the results. Yiwen Zhang and Lei Shi wrote the manuscript with input from all authors.

References

- [1] E. Yablonovitch, Photonic band-gap structures, *JOSA B* 10 (1993) 283–295.
- [2] J. D. Joannopoulos, S. G. Johnson, J. N. Winn, et al., *Photonic crystals: molding the flow of light*, Princeton university press, 2011.
- [3] S. Fan, J. D. Joannopoulos, Analysis of guided resonances in photonic crystal slabs, *Phys Rev B* 65 (2002) 235112.
- [4] R. V. Nair, R. Vijaya, Photonic crystal sensors: an overview, *Prog Quantum Electron* 34 (2010) 89–134.
- [5] W. L. Barnes, A. Dereux, T. W. Ebbesen, Surface plasmon subwavelength optics, *Nature* 424 (2003) 824.
- [6] D. Han, Y. Lai, J. Zi, et al., Dirac spectra and edge states in honeycomb plasmonic lattices, *Phys Rev Lett* 102 (2009) 123904.
- [7] Z. Fang, S. Thongrattanasiri, A. Schlather, et al., Gated tunability and hybridization of localized plasmons in nanostructured graphene, *ACS nano* 7 (2013) 2388–2395.
- [8] Z. Fang, Y. Wang, A. E. Schlather, et al., Active tunable absorption enhancement with graphene nanodisk arrays, *Nano Lett* 14 (2014) 299–304.
- [9] Y. Kang, S. Najmaei, Z. Liu, et al., Plasmonic hot electron induced structural phase transition in a mos2 monolayer, *Adv Mater* 26 (2014) 6467–6471.
- [10] R. A. Shelby, D. R. Smith, S. Schultz, Experimental verification of a negative index of refraction, *Science* 292 (2001) 77–79.
- [11] D. R. Smith, J. B. Pendry, M. C. Wiltshire, Metamaterials and negative refractive index, *Science* 305 (2004) 788–792.
- [12] D. Schurig, J. J. Mock, B. Justice, et al., Metamaterial electromagnetic cloak at microwave frequencies, *Science* 314 (2006) 977–980.
- [13] L. Feng, Y.-L. Xu, W. S. Fegadolli, et al., Experimental demonstration of a unidirectional reflectionless parity-time metamaterial at optical frequencies, *Nat Mater* 12 (2013) 108–113.
- [14] P. Moitra, Y. Yang, Z. Anderson, et al., Realization of an all-dielectric zero-index optical metamaterial, *Nat Photonics* 7 (2013) 791–795.
- [15] S.-y. Lin, J. Fleming, D. Hetherington, et al., A three-dimensional photonic crystal operating at infrared wavelengths, *Nature* 394 (1998) 251–253.
- [16] S. Noda, K. Tomoda, N. Yamamoto, et al., Full three-dimensional photonic bandgap crystals at near-infrared wavelengths, *Science* 289 (2000) 604–606.
- [17] O. Painter, R. Lee, A. Scherer, et al., Two-dimensional photonic band-gap defect mode laser, *Science* 284 (1999) 1819–1821.
- [18] H.-G. Park, S.-H. Kim, S.-H. Kwon, et al., Electrically driven single-cell photonic crystal laser, *Science* 305 (2004) 1444–1447.
- [19] J. Liu, P. Garcia, S. Ek, et al., Random nanolasing in the anderson localized regime, *Nat Nanotechnol* 9 (2014) 285–289.
- [20] S. Shen, A. Narayanaswamy, G. Chen, Surface phonon polaritons mediated energy transfer between nanoscale gaps, *Nano Lett* 9 (2009) 2909–2913.
- [21] M. De Zoysa, T. Asano, K. Mochizuki, et al., Conversion of broadband to narrowband thermal emission through energy recycling, *Nat Photonics* 6 (2012) 535.
- [22] A. P. Raman, M. A. Anoma, L. Zhu, et al., Passive radiative cooling below ambient air temperature under direct sunlight, *Nature* 515 (2014) 540.
- [23] S. Lal, S. Link, N. J. Halas, Nano-optics from sensing to waveguiding, *Nat Photonics* 1 (2007) 641.
- [24] X. Yu, L. Shi, D. Han, et al., High quality factor metalodielectric hybrid plasmonic–photonic crystals, *Adv Funct Mater* 20 (2010) 1910–1916.
- [25] Y. Fang, M. Sun, Nanoplasmonic waveguides: towards applications in integrated nanophotonic circuits, *Light-Sci Appl* 4 (2015) e294.
- [26] A. Chizari, S. Abdollahramezani, M. V. Jamali, et al., Analog optical computing based on a dielectric meta-reflect array, *Opt Lett* 41 (2016) 3451–3454.
- [27] Y. Shen, N. C. Harris, S. Skirlo, et al., Deep learning with coherent nanophotonic circuits, *Nat Photonics* 11 (2017) 441.
- [28] Y. Qu, H. Zhu, Y. Shen, et al., Inverse design of an integrated-nanophotonics optical neural network, *Sci Bull* 65 (2020) 1177–1183.
- [29] C. Lai, N. Kim, S. Utsunomiya, et al., Coherent zero-state and π -state in an exciton–polariton condensate array, *Nature* 450 (2007) 529.
- [30] L. Shi, T. Hakala, H. Rekola, et al., Spatial coherence properties of organic molecules coupled to plasmonic surface lattice resonances in the weak and strong coupling regimes, *Phys Rev Lett* 112 (2014) 153002.
- [31] L. Lu, J. D. Joannopoulos, M. Soljačić, Topological photonics, *Nat Photonics* 8 (2014) 821.
- [32] L. Lu, J. D. Joannopoulos, M. Soljačić, Topological states in photonic systems, *Nat Phys* 12 (2016) 626.
- [33] T. Cao, L. Fang, Y. Cao, et al., Dynamically reconfigurable topological edge state in phase change photonic crystals, *Sci Bull* 64 (2019) 814–822.
- [34] W.-J. Chen, S.-J. Jiang, X.-D. Chen, et al., Experimental realization of photonic topological insulator in a uniaxial metacrystal waveguide, *Nat Commun* 5 (2014) 1–7.
- [35] L. Ge, L. Wang, M. Xiao, et al., Topological edge modes in multilayer graphene systems, *Opt Express* 23 (2015) 21585–21595.
- [36] J.-W. Dong, X.-D. Chen, H. Zhu, et al., Valley photonic crystals for control of spin and topology, *Nat Mater* 16 (2017) 298–302.
- [37] X. Wu, Y. Meng, J. Tian, et al., Direct observation of valley-polarized topological edge states in designer surface plasmon crystals, *Nat Commun* 8 (2017) 1–9.
- [38] B. Zhen, C. W. Hsu, L. Lu, et al., Topological nature of optical bound states in the continuum, *Phys Rev Lett* 113 (2014) 257401.
- [39] B. Zhen, C. W. Hsu, Y. Igarashi, et al., Spawning rings of exceptional points out of dirac cones, *Nature* 525 (2015) 354–358.
- [40] H. Shen, B. Zhen, L. Fu, Topological band theory for non-hermitian hamiltonians, *Phys Rev Lett* 120 (2018) 146402.
- [41] H. Zhou, C. Peng, Y. Yoon, et al., Observation of bulk fermi arc and polarization half charge from paired exceptional points, *Science* 359 (2018) 1009–1012.
- [42] H. Gersen, T. Karle, R. Engelen, et al., Direct observation of bloch harmonics and negative phase velocity in photonic crystal waveguides, *Phys Rev Lett* 94 (2005) 123901.
- [43] R. J. Engelen, Y. Sugimoto, H. Gersen, et al., Ultrafast evolution of photonic eigenstates in k-space, *Nat Phys* 3 (2007) 401–405.
- [44] R. Houdré, C. Weisbuch, R. Stanley, et al., Measurement of cavity-polariton dispersion curve from angle-resolved photoluminescence experiments, *Phys Rev Lett* 73 (1994) 2043.
- [45] H. Ghaemi, T. Thio, D. e. a. Grupp, et al., Surface plasmons enhance optical transmission through subwavelength holes, *Phys Rev B* 58 (1998) 6779.
- [46] L. Shi, X. Liu, H. Yin, et al., Optical response of a flat metallic surface coated with a monolayer array of latex spheres, *Phys Lett A* 374 (2010) 1059–1062.
- [47] H. Gersen, M. F. García-Parajó, L. Novotny, et al., Influencing the angular emission of a single molecule, *Phys Rev Lett* 85 (2000) 5312.
- [48] M. A. Lieb, J. M. Zavislan, L. Novotny, Single-molecule orientations determined by direct emission pattern imaging, *JOSA B* 21 (2004) 1210–1215.
- [49] N. Le Thomas, R. Houdré, M. V. Kotlyar, Oothers, Exploring light propagating in photonic crystals with fourier optics, *JOSA B* 24 (2007) 2964–2971.
- [50] A. G. Curto, G. Volpe, T. H. Taminiau, et al., Unidirectional emission of a quantum dot coupled to a nanoantenna, *Science* 329 (2010) 930–933.
- [51] A. G. Curto, T. H. Taminiau, G. Volpe, et al., Multipolar radiation of quantum emitters with nanowire optical antennas, *Nat Commun* 4 (2013) 1–7.
- [52] C. I. Osorio, A. Mohtashami, A. F. Koenderink, K-space polarimetry of bullseye plasmon antennas, *Sci Rep* 5 (2015) 9966.
- [53] Y. Zhang, A. Chen, W. Liu, et al., Observation of polarization vortices in momentum space, *Phys Rev Lett* 120 (2018) 186103.
- [54] C. W. Hsu, B. Zhen, J. Lee, et al., Observation of trapped light within the radiation continuum, *Nature* 499 (2013) 188.
- [55] H. Zhou, B. Zhen, C. W. Hsu, et al., Perfect single-sided radiation and absorption without mirrors, *Optica* 3 (2016) 1079–1086.
- [56] H. M. Doeleman, F. Monticone, W. den Hollander, et al., Experimental observation of a polarization vortex at an optical bound state in the continuum, *Nat Photonics* 12 (2018) 397–401.

- [57] W. Liu, B. Wang, Y. Zhang, et al., Circularly polarized states spawning from bound states in the continuum, *Phys Rev Lett* 123 (2019) 116104.
- [58] L. Shi, X. Yuan, Y. Zhang, et al., Coherent fluorescence emission by using hybrid photonic-plasmonic crystals, *Laser Photon Rev* 8 (2014) 717–725.
- [59] S. Sun, K.-Y. Yang, C.-M. Wang, et al., High-efficiency broadband anomalous reflection by gradient meta-surfaces, *Nano Lett* 12 (2012) 6223–6229.
- [60] W. T. Chen, K.-Y. Yang, C.-M. Wang, et al., High-efficiency broadband meta-hologram with polarization-controlled dual images, *Nano Lett* 14 (2014) 225–230.
- [61] S. Wang, P. C. Wu, V.-C. Su, et al., A broadband achromatic metalens in the visible, *Nat Nanotechnol* 13 (2018) 227–232.
- [62] Z.-B. Fan, Z.-K. Shao, M.-Y. Xie, et al., Silicon nitride metalenses for close-to-one numerical aperture and wide-angle visible imaging, *Phys Rev Appl* 10 (2018) 014005.
- [63] J. Chen, C. Wan, Q. Zhan, Vectorial optical fields: recent advances and future prospects, *Sci Bull* 63 (2018) 54–74.
- [64] B. Wang, W. Liu, M. Zhao, et al., Generating optical vortex beams by momentum-space polarization vortices centred at bound states in the continuum, *Nat Photonics* (2020) 1–6.
- [65] R. Penrose, P. E. Jorgensen, The road to reality: A complete guide to the laws of the universe, *Math Intell* 28 (2006) 59–61.
- [66] J. Goodman, Introduction to Fourier optics, McGraw-hill, 2008.
- [67] M. Born, E. Wolf, Principles of optics: electromagnetic theory of propagation, interference and diffraction of light, Elsevier, 2013.
- [68] A. Ernst, On the estimation of aperture in the microscope, *JR Microsc Soc* 1 (1881) 388–423.
- [69] A. Small, Spherical aberration, coma, and the abbe sine condition for physicists who don't design lenses, *Am J Phys* 86 (2018) 487–494.
- [70] J. A. Kurvits, M. Jiang, R. Zia, Comparative analysis of imaging configurations and objectives for fourier microscopy, *JOSA A* 32 (2015) 2082–2092.
- [71] L. Shi, H. Yin, X. Zhu, et al., Direct observation of iso-frequency contour of surface modes in defective photonic crystals in real space, *Appl Phys Lett* 97 (2010) 251111.
- [72] E. C. Regan, Y. Igarashi, B. Zhen, et al., Direct imaging of isofrequency contours in photonic structures, *Sci Adv* 2 (2016) e1601591.
- [73] C. Luo, S. G. Johnson, J. Joannopoulos, et al., All-angle negative refraction without negative effective index, *Phys Rev B* 65 (2002) 201104.
- [74] A. Martinez, J. Marti, Negative refraction in two-dimensional photonic crystals: Role of lattice orientation and interface termination, *Phys Rev B* 71 (2005) 235115.
- [75] H. Kosaka, T. Kawashima, A. Tomita, et al., Superprism phenomena in photonic crystals, *Phys Rev B* 58 (1998) R10096.
- [76] J. Zi, X. Yu, Y. Li, et al., Coloration strategies in peacock feathers, *Proc Nat Acad Sci USA* 100 (2003) 12576–12578.
- [77] Y. Zhao, Z. Xie, H. Gu, et al., Bio-inspired variable structural color materials, *Chem Soc Rev* 41 (2012) 3297–3317.
- [78] Y. Zhang, B. Dong, A. Chen, et al., Using cuttlefish ink as an additive to produce non-iridescent structural colors of high color visibility, *Adv Mater* 27 (2015) 4719–4724.
- [79] D. Han, F. Wu, X. Li, et al., Transmission and absorption of metallic films coated with corrugated dielectric layers, *Appl Phys Lett* 89 (2006) 091104.
- [80] N. Le Thomas, R. Houdré, D. Beggs, et al., Fourier space imaging of light localization at a photonic band-edge located below the light cone, *Phys Rev B* 79 (2009) 033305.
- [81] J. Wang, A. Chen, M. Zhao, et al., Observation of optical states below the light cone with compound lattices, *OSA Continuum* 2 (2019) 1844–1850.
- [82] S. Fan, W. Suh, J. D. Joannopoulos, Temporal coupled-mode theory for the fano resonance in optical resonators, *JOSA A* 20 (2003) 569–572.
- [83] W. Suh, Z. Wang, S. Fan, Temporal coupled-mode theory and the presence of non-orthogonal modes in lossless multimode cavities, *IEEE J Quantum Electron* 40 (2004) 1511–1518.
- [84] C. W. Hsu, B. Zhen, M. Soljačić, et al., Polarization state of radiation from a photonic crystal slab, *arXiv preprint arXiv:1708.02197* (2017).
- [85] J. Jin, X. Yin, L. Ni, et al., Topologically enabled ultrahigh-q guided resonances robust to out-of-plane scattering, *Nature* 574 (2019) 501–504.
- [86] Z. Liu, Y. Xu, Y. Lin, et al., High-q quasibound states in the continuum for nonlinear metasurfaces, *Phys Rev Lett* 123 (2019) 253901.
- [87] C. W. Hsu, B. Zhen, A. D. Stone, et al., Bound states in the continuum, *Nat Rev Mater* 1 (2016) 1–13.
- [88] J. Korger, T. Kolb, P. Banzer, et al., The polarization properties of a tilted polarizer, *Opt Express* 21 (2013) 27032–27042.
- [89] L. Mandel, E. Wolf, Coherence properties of optical fields, *Rev Mod Phys* 37 (1965) 231.
- [90] A. W. Rodriguez, O. Ilic, P. Bermel, et al., Frequency-selective near-field radiative heat transfer between photonic crystal slabs: a computational approach for arbitrary geometries and materials, *Phys Rev Lett* 107 (2011) 114302.
- [91] T. Sannomiya, T. E. Balmer, C. Hafner, et al., Optical sensing and determination of complex reflection coefficients of plasmonic structures using transmission interferometric plasmonic sensor, *Rev Sci Instrum* 81 (2010) 053102.
- [92] Y. Guo, M. Xiao, S. Fan, Topologically protected complete polarization conversion, *Phys Rev Lett* 119 (2017) 167401.
- [93] M. Khorasaninejad, W. T. Chen, R. C. Devlin, et al., Metalenses at visible wavelengths: Diffraction-limited focusing and subwavelength resolution imaging, *Science* 352 (2016) 1190–1194.
- [94] Y. Guo, M. Xiao, Y. Zhou, et al., Arbitrary polarization conversion with a photonic crystal slab, *Adv Opt Mater* (2019) 1801453.
- [95] S. Shen, T. Liu, J. Guo, Optical phase-shift detection of surface plasmon resonance, *Appl Optics* 37 (1998) 1747–1751.
- [96] N. Yu, P. Genevet, M. A. Kats, et al., Light propagation with phase discontinuities: generalized laws of reflection and refraction, *Science* 334 (2011) 333–337.
- [97] A. Patil, P. Rastogi, Approaches in generalized phase shifting interferometry, *Opt Lasers Eng* 43 (2005) 475–490.
- [98] P. Carré, Installation et utilisation du comparateur photoélectrique et interférentiel du bureau international des poids et mesures, *Metrologia* 2 (1966) 13.
- [99] N. C. Zambon, P. St-Jean, M. Miličević, et al., Optically controlling the emission chirality of microlasers, *Nat Photonics* 13 (2019) 283–288.
- [100] Y. Li, S. Kita, P. Muñoz, et al., On-chip zero-index metamaterials, *Nat Photonics* 9 (2015) 738–742.
- [101] I. Liberal, N. Engheta, Near-zero refractive index photonics, *Nat Photonics* 11 (2017) 149–158.
- [102] H. Tang, C. DeVault, P. Camayd-Munoz, et al., Low-loss zero-index materials, *arXiv preprint arXiv:2004.01818* (2020).
- [103] J. B. Pendry, Negative refraction makes a perfect lens, *Phys Rev Lett* 85 (2000) 3966.
- [104] J. Witzens, M. Loncar, A. Scherer, Self-collimation in planar photonic crystals, *IEEE J Sel Top Quantum Electron* 8 (2002) 1246–1257.
- [105] Z. Lu, S. Shi, J. A. Murakowski, et al., Experimental demonstration of self-collimation inside a three-dimensional photonic crystal, *Phys Rev Lett* 96 (2006) 173902.
- [106] D. W. Prather, S. Shi, J. Murakowski, et al., Self-collimation in photonic crystal structures: a new paradigm for applications and device development, *J Phys D-Appl Phys* 40 (2007) 2635.
- [107] A. F. Matthews, S. K. Morrison, Y. S. Kivshar, Self-collimation and beam splitting in low-index photonic crystals, *Opt Commun* 279 (2007) 313–319.
- [108] J. Topolancik, B. Ilic, F. Vollmer, Experimental observation of strong photon localization in disordered photonic crystal waveguides, *Phys Rev Lett* 99 (2007) 253901.
- [109] C. Li, M. Zhao, X. Zhou, et al., Janus structural color from a 2d photonic crystal hybrid with a fabry-perot cavity, *Adv Opt Mater* 6 (2018) 1800651.
- [110] B. Lv, T. Qian, H. Ding, Angle-resolved photoemission spectroscopy and its application to topological materials, *Nat Rev Phys* 1 (2019) 609–626.
- [111] Y. Xu, Y. Huang, X. Cui, et al., Observation of a ubiquitous three-dimensional superconducting gap function in optimally doped $\text{Ba}_{0.6}\text{K}_{0.4}\text{Fe}_2\text{As}_2$, *Nat Phys* 7 (2011) 198–202.
- [112] V. N. Strocov, M. Shi, M. Kobayashi, et al., Three-dimensional electron realm in VSe_2 by soft-X-ray photoelectron spectroscopy: Origin of charge-density waves, *Phys Rev Lett* 109 (2012) 086401.
- [113] A. Damascelli, Z. Hussain, Z.-X. Shen, Angle-resolved photoemission studies of the cuprate superconductors, *Rev Mod Phys* 75 (2003) 473.

[114] A. Morey, Nist policy on metrological traceability (2010).